Fault-Plane Determination of the 4 January 2020 Offshore Pearl River Delta Earthquake and Its Implication for Seismic Hazard Assessment

Han Chen[1], Xiaohui He[2,3], Hongfeng Yang[*1,4], and Jiangyang Zhang[4]

Abstract

On 4 January 2020, an M_L 3.5 earthquake occurred in the Pearl River Estuary (PRE) and was felt at a distance of more than 200 km. According to the China Earthquake Networks Center, this event has been the only M > 3 earthquake within the PRE since 1900. The Guangdong–Hong Kong–Macau Bay Area (GHMBA) surrounding the PRE is one of China's most critical financial circles, and coastal earthquake hazard has become an increasing concern. Investigating the source parameter and causative fault of this earthquake is helpful for seismic hazard estimation and mitigation in the GHMBA. In this study, we first determined the focal mechanism of the mainshock using the cut-and-paste method. We then used the sliding-window cross-correlation method to detect foreshocks and aftershocks before relocating the earthquakes. Finally, we conducted forward modeling to retrieve the rupture directivity of the mainshock, using waveforms of one aftershock as empirical Green's functions. The results demonstrate that this earthquake was an M_w 3.7 strike-slip event, with a focal depth of 10 km. The rupture direction of the mainshock was 78°, consistent with the northeast-east-trending fault system in the region. The identified source fault confirmed a seismogenic segment of the northeast-east-trending fault system in the PRE, which is the primary source of seismic hazard in the area.

Cite this article as Chen, H., X. He, H. Yang, and J. Zhang (2021). Fault-Plane Determination of the 4 January 2020 Offshore Pearl River Delta Earthquake and Its Implication for Seismic Hazard Assessment, *Seismol. Res. Lett.* **92**, 1913–1925, doi: 10.1785/0220200232.

Supplemental Material

Introduction

Earthquakes are among the most destructive natural hazards, causing significant damage to human life, property safety, and social stabilization. At coastal deltas where populous cities are widely distributed, not only do earthquakes inland lead to great damages (Saito *et al.*, 2004; Galvis *et al.*, 2017; Sepahi *et al.*, 2020), but also offshore earthquakes pose significant threats by generating strong ground shaking and sometimes triggering tsunamis (Ghobarah *et al.*, 2006; Mimura *et al.*, 2011). Furthermore, the wide-spreading unconsolidated sediment (Guo *et al.*, 1995) at coastal deltas may amplify the ground motions and intensify damage (Atkinson and Cassidy, 2000; Hunter and Christian, 2001; Assimaki and Jeong, 2013). The potential hazard of earthquakes on offshore causative faults thus has become an increasing concern. Investigating offshore causative faults becomes critical because they provide valuable information on the potential scale and location of future earthquakes.

Previous investigations of offshore faults have been carried out mainly by analyzing topography, stratigraphic changes, gravity and/or magnetic anomalies, and satellite images (Liu, 1985; Fichler *et al.*, 1997; Tan *et al.*, 2000; Bhattacharyya *et al.*, 2009). Studies based on seismic activities and surface ruptures of onshore faults also have inferred the distribution and historical activities of offshore faults (Dong, 2016; Yu *et al.*, 2016). However, it is difficult for these studies to give critical parameters of offshore faults without direct on-fault observational evidence. In comparison, studies using seismic reflection data have revealed the location, continuity, and geometry of offshore fault zones (Stefatos *et al.*, 2002; Hsiao *et al.*, 2004; Li *et al.*, 2006; Cao *et al.*, 2018; Xia *et al.*, 2018). This approach works well for dip-slip faults with significant vertical displacements, but identifying strike-slip faults becomes more difficult. In addition, it is still limited in

1. Earth System Science Programme, Faculty of Science, The Chinese University of Hong Kong, Shatin, Hong Kong, China; 2. Guangdong Provincial Key Lab of Geodynamics and Geohazards, School of Earth Sciences and Engineering, Sun Yat-sen University, Guangzhou, China; 3. Southern Laboratory of Ocean Science and Engineering, Zhuhai, China; 4. Shenzhen Research Institute, The Chinese University of Hong Kong, Shenzhen, China

*Corresponding author: hyang@cuhk.edu.hk

mapping faults in a shallow water area because of the limitation on data acquisition. For instance, a few faults were inferred near the Pearl River Estuary (PRE) (e.g., Liu, 1985), which is located in the central area of the Guangdong–Hong Kong–Macau Bay Area (GHMBA; Fig. 1b). However, except for a small region that has been surveyed comprehensively (Li *et al.*, 2006; Fig. 1b, the black box) and the Littoral fault zone (LFZ) that developed farther offshore, critical fault parameters, including strike, dip angle, and depth extent as well as precise position, are unknown for numerous faults with smaller scales.

An essential consideration for hazard estimation of offshore faults is the potential for a through-going rupture and the maximum magnitude of future earthquakes (Grant and Shearer, 2004). Based on the probabilistic seismic hazard analysis, the maximum moment magnitude of earthquakes in the PRE area is around 6.5 and even reaches 7.5 near the Dangang Island, slightly outside the PRE (Lee *et al.*, 2000; Pappin *et al.*, 2015). Near-coast earthquakes with such magnitudes can be undoubtedly destructive, particularly in delta areas with large populations and intensive economics, such as the GHMBA. Considering the large population (70 million), tremendous economic value (Gross Domestic Product (GDP) > 8 trillion CNY), and numerous infrastructures (e.g., the Hong Kong–Zhuhai–Macau bridge, the longest across-bay bridge in the world, and lots of offshore oil platforms), seismic hazard assessment and mitigating the risks of potential large earthquakes are essential in the area. Thus, the precise estimation of the maximum magnitude of potential PRE earthquakes is critical. However, direct evidence for estimating the maximum magnitude of PRE earthquakes is still absent. Therefore, mapping offshore causative faults is necessary in the region because it could provide valuable information on the potential scale and location of future earthquakes.

On 4 January 2020, an M_L 3.5 earthquake occurred in the PRE and was felt at a distance of more than 200 km. This earthquake did not happen on the well-known LFZ but occurred closer to populous cities with numerous high-rise buildings, with the epicenter within 30 km of Hong Kong, 40 km of Macau, 55 km of Zhuhai, and 65 km of Shenzhen. In this study, we determined source parameters and rupture directivity of the mainshock to identify the seismogenic fault using all available local and regional seismic network data. The results can be used to improve the seismic hazard assessment in the region.

Tectonic Setting

Our study area is located on the northern continental margin of the South China Sea (SCS), an intensive neotectonics activity zone since the Miocene Epoch (Zhao *et al.*, 2004). It was a convergent margin during the Mesozoic era (Li *et al.*, 2018) and became extensional possibly due to the subduction direction reversal of Proto-SCS (Li *et al.*, 2020). The stress field in the northern SCS inferred from borehole measurements, earthquake focal mechanisms, and numerical modeling is mixed, with the middle region (close to the PRE) showing tensional stress. The principal stress axes change from west to east (i.e., northeast–southwest close to Hainan, north–south near PRE, and northwest-west–southeast-east near Taiwan) (Wei *et al.*, 1996; Chen *et al.*, 2014). There are three sets of fault zones trending mainly in the northeast, northeast-east, and northwest directions (Fig. 1b) that dominate the structural characterization of this region (Pigott and Ru, 1994; Liu *et al.*, 1997). The northeast-trending faults were mainly formed in the Mesozoic and got extensively activated during the Yanshanian orogeny. They controlled the northeast-trending near-parallel mountains and valleys (Zhang and Wu, 1994). The northeast-east-trending faults were also formed at Mesozoic and reactivated as tensional faults during the seafloor spreading of the SCS. These faults cut into the deep crust and dominated the distribution and direction of sedimentary basins in the northern SCS (Tan *et al.*, 2000). The northwest-trending faults were superficial faults mainly formed during the late Yanshanian or Himalayan orogeny and became more active recently (Liu, 1986; Zhang and Wu, 1994; Li *et al.*, 2006).

A series of earthquakes have taken place in these fault systems (Fig. 1a). The 19 March 1962 M_w 6.1 Heyuan earthquake and the 26 July 1969 M_w 6.4 Yangjiang earthquake occurred in the northeast-trending faults system. The northeast-east-trending faults are more active, with several **M** > 7 earthquakes (13 July 1605 M_w 7.5 Qiongzhou earthquake and 13 February 1918 M_w 7.5 Nan'ao earthquake) and moderate events (23 June 1874 M_w 5.8 Dangan Island earthquake, 15 May 1911 M_w 6 Honghai Bay earthquake, and 14 September 2006 M_L 4.0 Dangan Island earthquake). The northwest-trending faults are in a relatively small scale, with the largest documented event being the 11 August 1905 M_w 5.5 Macau earthquake (Free *et al.*, 2004; Megawati *et al.*, 2004).

The intersection of these sets of faults complicates the seismogenic process in the area. The northwest-trending faults cut and offset another two sets of faults, and the intersections became stress concentrators and caused abnormal stress buildup that might generate earthquakes (Gangopadhyay and Talwani, 2003). Zhang and Wu (1994) suggested that the structural dislocation caused by fault offsets changed the stress state of northeast-east-trending faults and led to earthquakes. For instance, the 1874 **M** 5.8 and the 2006 M_L 4.0 Dangan Island earthquakes were adjacent to the intersection of the northeast- and northwest-trending faults (Xia *et al.*, 2018).

The LFZ is a set of northeast-east-trending right-lateral strike-slip faults located in the central portion of the northern continental margin of the SCS (Fig. 1a), approximately along the 30–50 m isobath of offshore PRE (Liu, 1985), dipping southeast (Zhao *et al.*, 2004; Cao *et al.*, 2018). Gravity and geomagnetism anomalies are significant along the fault zone (Hao *et al.*, 2002). Active source seismic profiles show that the crustal structure in the northern and southern LFZs are different, suggesting that it is the boundary between the normal and thinned continental crust (Zhao *et al.*, 2004; Xia *et al.*, 2010).

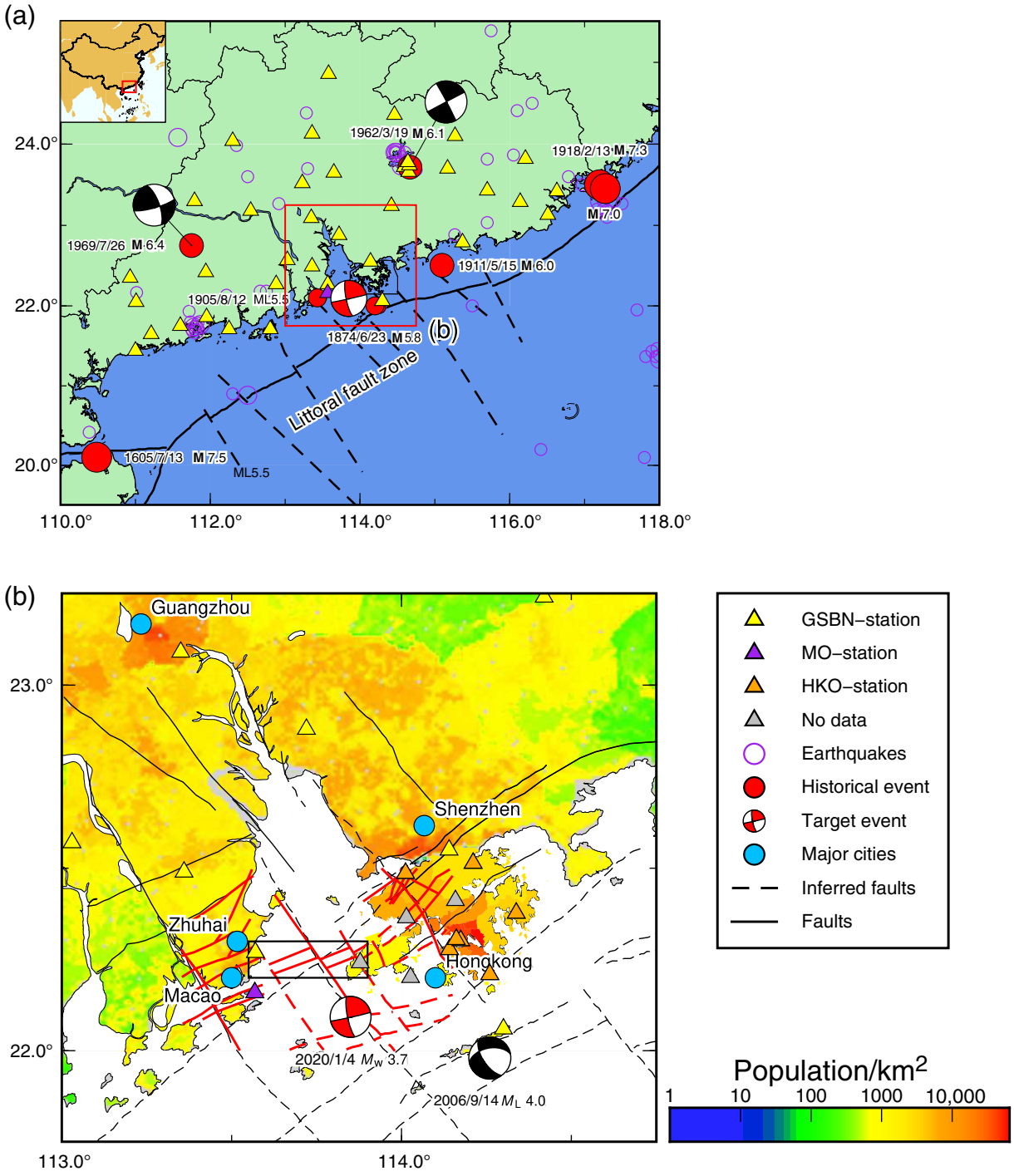

Figure 1. (a) Locations of seismograph stations in Guangdong Province and Macau and the distribution of historical earthquakes (red dots) and catalog events (purple circles). The earthquake catalog comes from Guangdong Seismological Bureau Network (GSBN). The red focal mechanism plots (not in scale) represent the focal mechanisms of the mainshock (red) and historical earthquakes (black). Thick black lines indicate the Littoral fault zone, and dashed lines indicate the inferred faults. Yellow triangles represent GSBN stations, and the purple triangle represents Macau station. The inset at the top left represents the location of the study region in china. (b) The population density and major cities distribution of the Pearl River Estuary. Blue dots represent major cities. The focal mechanism plots have the same meaning as panel (a). Orange triangles represent Hong Kong Observatory Network (HKO) stations with available data, and gray triangles represent stations without available data. Solid lines show identified faults (black: Cao *et al.*, 2018; red: Li *et al.*, 2006), and dashed lines indicate inferred faults. The black box indicates the study region in Li *et al.* (2006). The background color indicates the population density, sourced from Fu *et al.* (2014) and the Census and Statistics Department of Hong Kong (see Data and Resources). The color version of this figure is available only in the electronic edition.

Furthermore, the LFZ was cut into segments by several northwest-trending faults. It has been suggested that both the LFZ and the northwest-trending faults control the seismicity in the offshore PRE (Lee and Workman, 1996) and that their intersections might dominate the generation of great earthquakes (Xu *et al.*, 2006; Sun *et al.*, 2012).

Historical earthquakes with magnitudes larger than 7 were reported in the eastern and western LFZs (Xia *et al.*, 2018), whereas the segment near the offshore PRE was considered a seismic gap (Fig. 1a), with the potential seismic intensity scale of 8 (Guangdong Seismological Bureau, 2011; Pappin *et al.*, 2015). The offshore PRE was suggested to have the potential to produce earthquakes with magnitudes larger than 7 (Chau *et al.*, 2004; Megawati, 2007; Chen *et al.*, 2009). Yet, many faults that are capable of generating moderate to strong earthquakes remain unclear in their geometries and faulting mechanisms. Therefore, mapping faults in the region is of great importance in terms of disaster estimation and mitigation (Yang, 2015; Xia *et al.*, 2018).

Data and Results

Seismic data used in this study consist of records at the seismic stations of Guangdong Seismological Bureau Network (GSBN), Hong Kong Observatory Network (HKO), and Macau Observatory Network (MO), which include both seismometers and accelerometers (Fig. 1a,b). The GSBN dataset includes 38 stations with sampling rates of 100 samples per second. The HKO dataset contains seven seismometers with sampling rates of 100 samples per second (except for the HKPS station with a sampling rate of 50 samples per second) and five accelerometers with sampling rates of 100 samples per second. The MO dataset includes one seismometer with a sampling rate of 100 samples per second. We used seismometer data for earthquake detection and focal mechanism determination, and all data for earthquakes relocation. Stations within 200 km of the epicenter were used in rupture directivity analysis.

Double-couple solution

The double-couple solution was computed using the cut-and-paste (CAP) method (Zhu and Helmberger, 1996). The seismograms were decomposed and separated into different time windows (e.g., *Pnl* and surface wave), allowing for separate time shifts to account for the effects of an imperfect velocity model. Broadband waveform data from all of the previous networks were used, except for data with unclear *P*-wave onsets and problematic amplitudes. The time-window length was 20 s for *Pnl* phases and 60 s for surface waves. We applied a frequency band from 0.05 to 0.2 Hz for the *Pnl* phases and from 0.03 to 0.1 Hz for the surface waves.

We then modified a 1D crustal velocity model of South China (Fan *et al.*, 1990) on top of the 1D IASP91 global velocity model (Kennett and Engdahl, 1991) (Table 1). We computed the Green's functions using a Haskell propagator matrix method (Zhu and Rivera, 2002) based on the velocity model. We set equal weights for the *Pnl* and surface waves for CAP inversion. The result of waveform inversion showed that the earthquake was a strike-slip event, with two nodal planes (NPs) 78°/88°/169° (NP1) and 168°/79°/2° (NP2). The moment magnitude was ~3.7, with a focal depth of 10 km (Fig. 2a,b).

TABLE 1
Velocity Model Used in This Study

Depth (km)	V_P (km/s)	V_S (km/s)
0	6.01	3.43
21.4	6.88	3.93
32.4	7.98	4.56
310	8.66	4.95

We then performed uncertainty analysis of the CAP inversion result using a bootstrapping inversion method (Tichelaar and Ruff, 1989; Sheng *et al.*, 2020), in which stations were randomly selected from the station pool (21 stations in total), allowing multiple sampling. Specifically, we sampled one station from the pool each time and repeated the sampling 21 times. The 21 sampled stations (with repeating ones) were used for CAP inversion, and more weight given for stations that were sampled multiple times. We then repeated the process 1000 times (Fig. 2c). Histogram of the 1000 results showed a highly concentrated distribution in the strike, but with more scattered results in the dip and rake (Fig. S1, available in the supplemental material to this article). Based on these 1000 focal mechanisms, we employed a particle swarm optimization algorithm (Fukuyama, 2002) to search for the best solution by minimizing the sum of the minimum rotation angle (MRA) (Yu *et al.*, 2009), with the following procedure.

When using the coordinate of the *P*-, *B*-, and *T*-axes of a focal mechanism solution, the difference between two solutions is described by the MRA:

$$(\theta_{mn})_{\min} = \arccos\left(\frac{\alpha + abs(\beta + \gamma) - 1}{2}\right), (0 \le (\theta_{mn})_{\min} \le 120), \quad (1)$$

in which m and n are two coordinate systems, $(\theta_{mn})_{\min}$ is the MRA between the two coordinate systems, and α, β, and γ are the maximum, minimum, and median of the dot product of *P*-, *B*-, and *T*-axes of two solutions (i.e., $P_m \cdot P_n \cdot T_m \cdot T_n \cdot B_m \cdot B_n$), respectively. The optimal solution showed a strike of 167.18°, dip of 78.87°, and rake of 2.86°, which are very close to our CAP inversion result (Fig. 2c). The standard deviation of the MRA between the average solution with all inversion results is 4.6°, the double of which (9.2°) reflects the uncertainty of our CAP result.

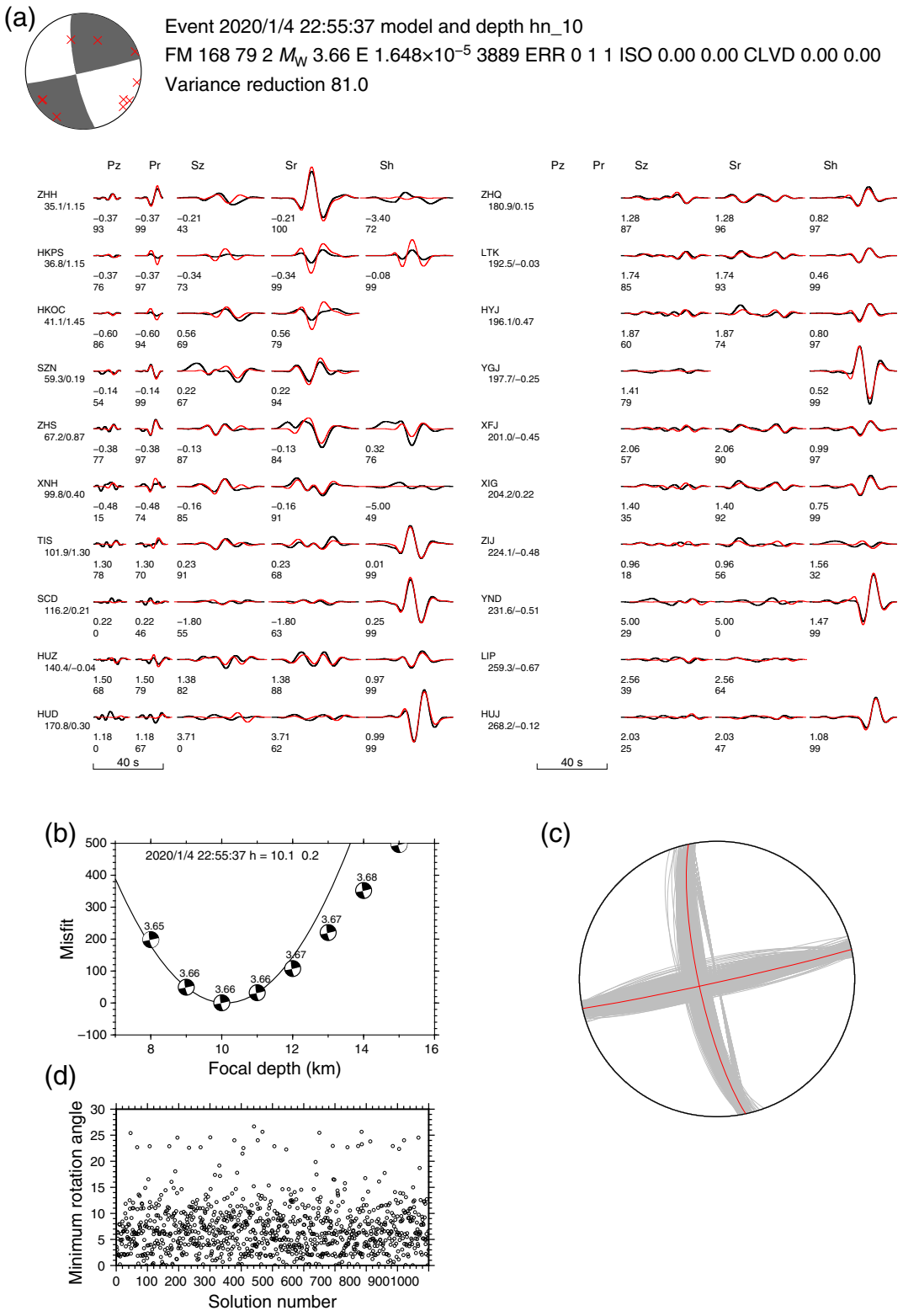

Figure 2. (a) Waveform inversion result for the mainshock. Black and red waveforms are observed and synthetic seismograms, respectively. The numbers below the station names are epicentral distances and azimuths. The numbers below the seismograms are time shifts and cross-correlation (CC) coefficients in percent. Stations used in the inversion are indicated as crosses on the focal mechanism plot. (b) Waveform misfit versus centroid depth. (c) Results of bootstrapping inversion. Gray lines indicate the focal planes of 1000 times bootstrapping inversion results, and red lines indicate the focal planes of cut-and-paste (CAP) inversion. (d) The distribution of minimum rotation angle (MRA) between the bootstrapping inversion results with the average solution. CLVD, calibrated linear vector dipole. The color version of this figure is available only in the electronic edition.

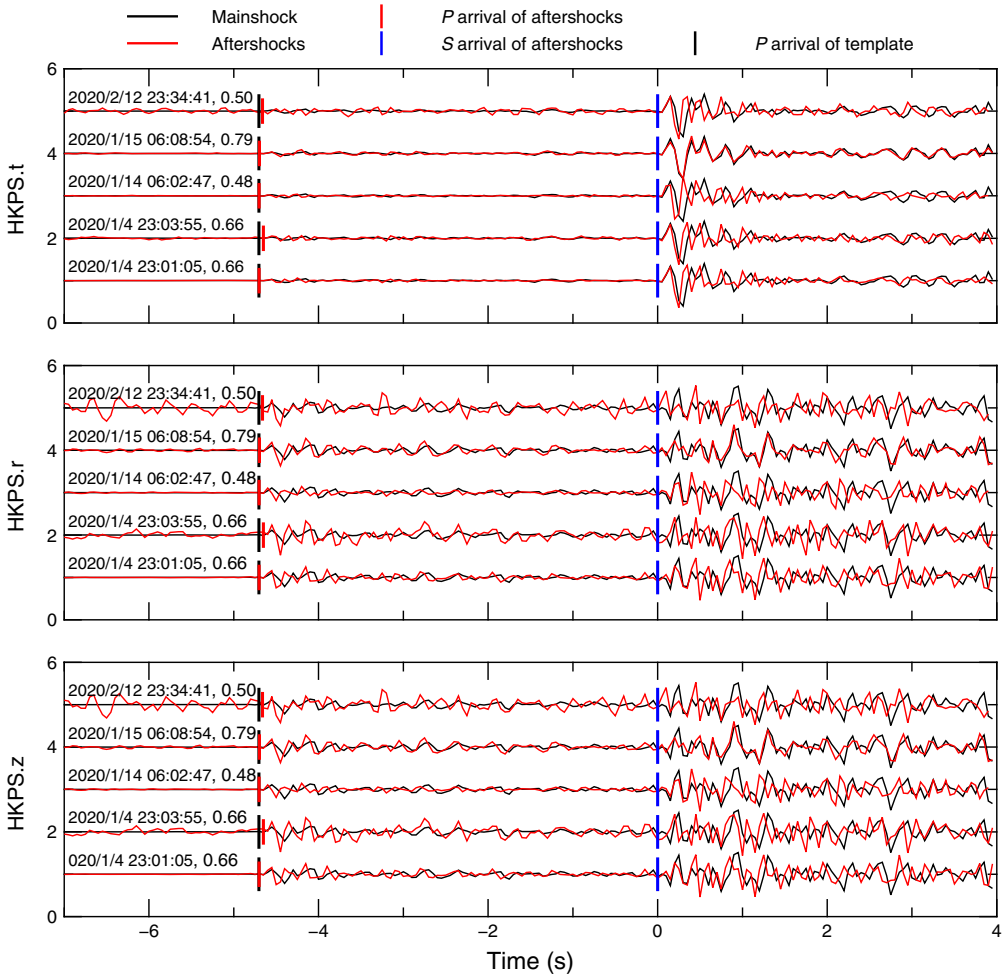

Figure 3. Three-component waveforms comparison of the mainshock (black traces) and aftershocks (red traces). Waveforms are aligned according to *S*-wave arrival times. The short vertical lines mark the *P*-wave arrivals of the mainshock (black) and aftershocks (red) and the *S*-wave arrivals of all of the events (blue). The numbers above waveforms are the origin times of aftershocks and simultaneous CC coefficients on three components. The color version of this figure is available only in the electronic edition.

We also tested different velocity models, including the IASP91 crustal velocity model and a crustal velocity model of the Guangdong area. These velocity models differed most in shallow depths and became similar in greater depths (Fig. S2). The solutions did not change much using these velocity models. The dips of the NP from all solutions were the same, whereas there was only 1° difference in the strike direction and 5° difference in the rake angle.

Aftershock detection

To find more earthquakes, we performed earthquake detection using the Sliding-window Cross-correlation (SCC) detection technique (Yang *et al.*, 2009). SCC detection on multiple stations may minimize false alarms, which is desired in regions with a large number of seismicity. However, to detect as many nearby earthquakes as possible (Zhu *et al.*, 2019), we carried out the SCC detection on a single station (i.e., HKPS station), which is the closest long-term station with accessible continuous data. We used the waveforms of the mainshock as the template, spanning from 2 s before to 10 s after *P*-wave arrivals. We obtained continuous waveform data one month before to four months after the mainshock, saved them in one day long recordings, and applied a band-pass filter from 2 to 8 Hz. Then, we applied the SCC detection in three channels simultaneously to reduce false alarms, with a threshold of the SCC coefficient of 0.4.

We did not find any foreshocks in the time window. In comparison, we found five aftershocks, two of which were reported by networks. Waveforms of the five aftershocks were similar to those of the mainshock (Fig. 3), indicating that they originated from the same fault and had similar focal mechanisms.

We also determined the magnitudes of the detected earthquakes by:

$$M_{\text{new}} = M_{\text{template}} + C \log_{10} R, \quad (2)$$

in which $M_{\text{template}} = 3.7$, C is a constant, and R is the amplitude ratio between the new event and the template (Yang *et al.*, 2009; Schaff and Richards, 2014; Meng *et al.*, 2018). Here, we took $C = 2/3$ because we adopted the moment magnitude of the template event (Hanks and Boore, 1984; Shelly *et al.*, 2016).

The vertical-component profiles of the mainshock and aftershocks were shown in Figure 4a–f. *P*- and *S*-wave arrivals of the mainshock and aftershock numbers 1, 3, and 4 can be identified at almost all stations, whereas the arrivals of the aftershock numbers 2 and 6 were only visible at stations with distances less than 150 km.

Earthquake relocation

We then relocated these earthquakes using the HYPOINVERSE-2000 program (Klein, 2002) based on their *P*- and *S*-wave travel times. We manually picked their *P*- and *S*-wave arrivals on all

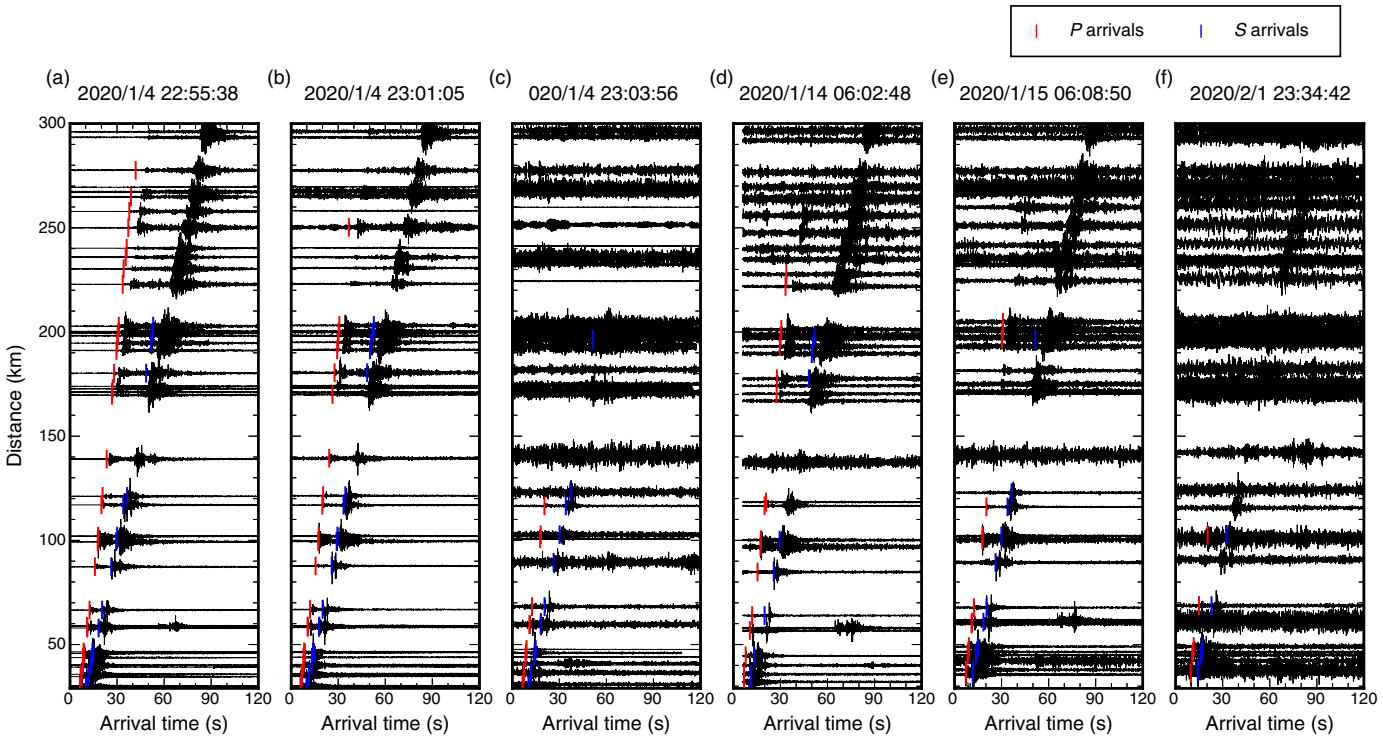

Figure 4. Time–distance profiles of the (a) mainshock and (b–f) aftershocks aligned with their original times. Red and blue bars indicate the picked *P*- and *S*-wave travel times, respectively. The color version of this figure is available only in the electronic edition.

available stations after applying a band-pass filter from 2 to 8 Hz. We only selected impulsive phases to reduce the uncertainties of arrival picking, having 111 *P*-wave arrivals and 83 *S*-wave arrivals in total. All events were relocated after 7–8 iterations with uncertainties in horizontal locations and focal depths smaller than 1 km, except for the smaller aftershocks.

We further improved the location results using the double-difference relocation algorithm (HypoDD) (Waldhauser and Ellsworth, 2000). *P*- and *S*-wave differential times between any two events at stations were obtained through waveform cross correlation (CC) with a CC coefficient threshold of 0.4, complemented by the manually picked *P* and *S* waves. Then, 153 *P*-phase pairs and 114 *S*-phase pairs based on picked arrivals and 81 *P*-phase pairs and 76 *S*-phase pairs from CC were used. All events were successfully relocated, and the uncertainties were significantly reduced, with the root-mean-square travel time residual decreasing from 1.2 to 0.1 s. The relocation errors were around 100–200 m (Table 2).

The locations of all events were adjacent to the intersection of two inferred faults (Fig. 5a–d). The interevent distances were comparable with the uncertainties in locations. Therefore, we cannot infer which fault was responsible for these earthquakes, given the small number of events.

Rupture directivity analysis

We then analyzed the rupture directivity of the mainshock via the azimuthal variation of source duration to determine the causative fault. The waveforms of a reference event can be adopted as empirical Green's functions (EGFs) to approximate the path effect (Hartzell, 1978). Then, the relative source duration of the mainshock at different stations can be obtained by deconvolving with the EGFs or through a forward-modeling approach (e.g., Tan and Helmberger, 2010).

For strike-slip events, the azimuthal variation of relative source durations at local stations is approximated as follows:

$$t_d(az) = 2 \times t_r + \frac{L}{V_f} - \frac{L}{V_P} \times \cos(\mathrm{az} - \mathrm{stk}), \quad (3)$$

in which $t_d(az)$ is the relative source duration with the azimuth of az, t_r is the differential rise time between the mainshock and reference event, L is the rupture length, V_f is the rupture velocity, V_P is the *P*-wave velocity, and stk is the strike of either NP of the moment tensor solution.

The waveforms of the first aftershock (4 January 2020 23:01:05 M_w 3.0) were highly correlated with the mainshock (Fig. 2a) with an averaged CC coefficient of 0.703 on three components in a time window spanning from 2 s before to 10 s after the *S*-wave arrivals. We also low-pass filtered the vertical waveforms with a corner frequency of 5 Hz and found a higher CC coefficient (0.85) of the low-pass filtered waveforms between two events (Fig. S3). In addition, we manually picked the *P*-wave polarities at regional stations, which showed good consistency with the focal mechanism of the mainshock, indicating that the fault solution is similar to the mainshock

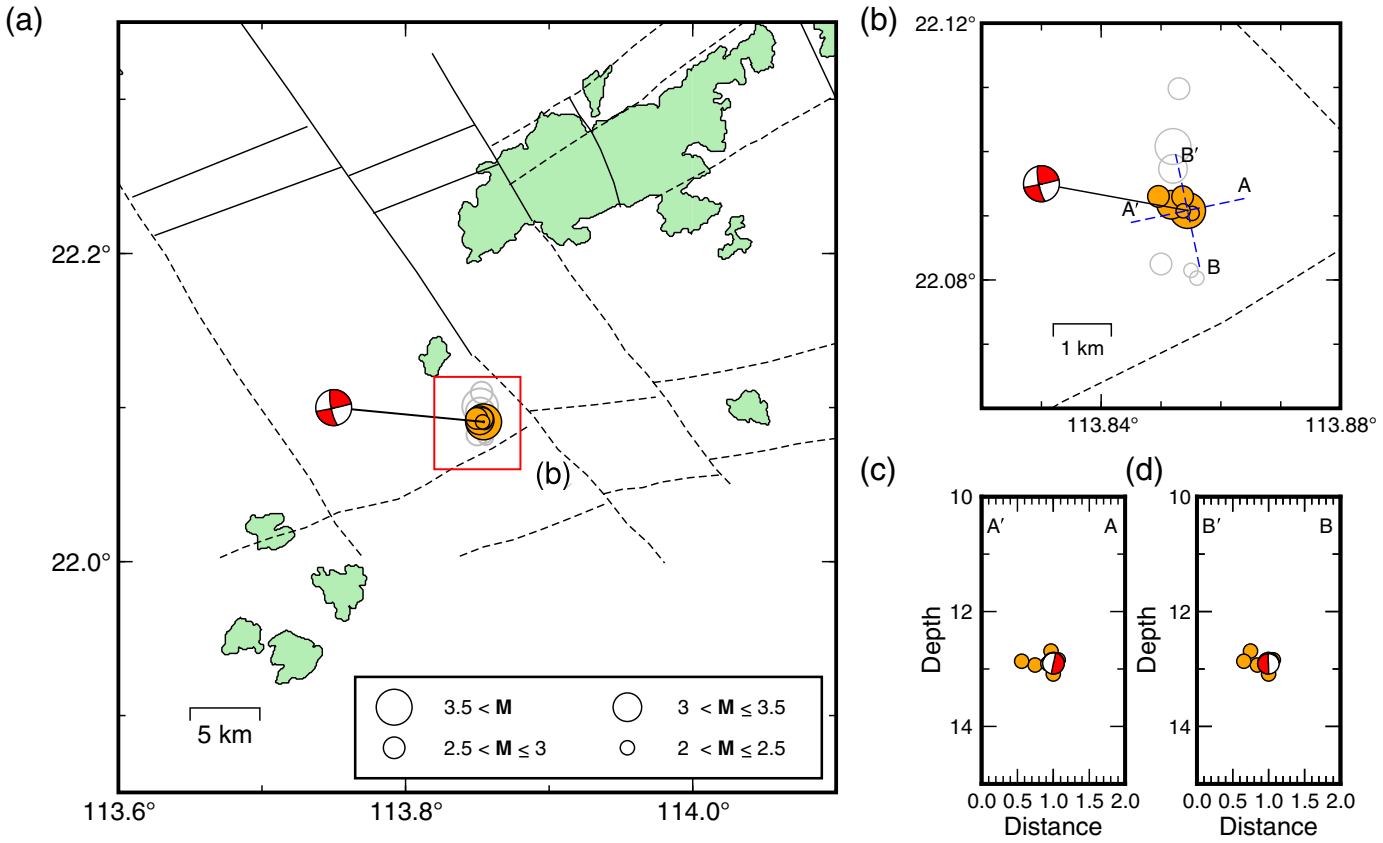

(Fig. S4). Therefore, the waveforms of the first aftershock provided ideal EGFs for the mainshock. In total, 25 local stations (epicentral distance <200 km) recorded both the mainshock and the reference event. We applied a low-pass filter of 5 Hz to retain the finite-source feature of the mainshock. We then picked *P* onset manually and kept 14 stations with clear *P* onset (Fig. 6a,b). The apparent source durations at stations to the northwest were significantly longer than stations to the northeast for the mainshock, indicating a rupture direction toward the northeast. Details about the selection of the filtering frequency band are provided in the supplemental material (Supplementary Note 1).

Figure 5. (a) Locations of the mainshock and aftershocks obtained using the hypoDD method (orange dots) and HYPOINVERSE method (gray circles). The focal mechanism plot shows the focal mechanism of the mainshock. Dashed and solid lines indicate the inferred and identified faults, respectively. (b) Zoom-in view of the earthquake locations. (c) Cross-section view of earthquakes with a strike the same as nodal plane (NP1) (78°). The focal mechanism plot indicates the mainshock, and orange dots indicate aftershocks. Panel (d) is the same as panel (c) but with a strike the same as NP2 (168°). The color version of this figure is available only in the electronic edition.

TABLE 2
Earthquakes Locations

Date and Time of Event (yyyy/mm/dd hh:mm:ss)	Longitude (°E)	Latitude (°N)	Depth (km)	Magnitude (M_w)	Horizontal Error (m)	Vertical Error (m)
2020/1/4 22:55:38	113.854	22.091	13.09	3.7	25.7	52.2
2020/1/4 23:01:05	113.852	22.092	12.93	3.0	17.7	46.0
2020/1/4 23:03:56	113.855	22.090	12.84	2.2	39.5	61.8
2020/1/14 06:02:48	113.854	22.093	12.69	2.8	56.1	84.0
2020/1/15 06:09:50	113.850	22.093	12.87	2.6	21.4	52.3
2020/2/12 23:34:42	113.854	22.091	12.91	2.0	25.1	204.9

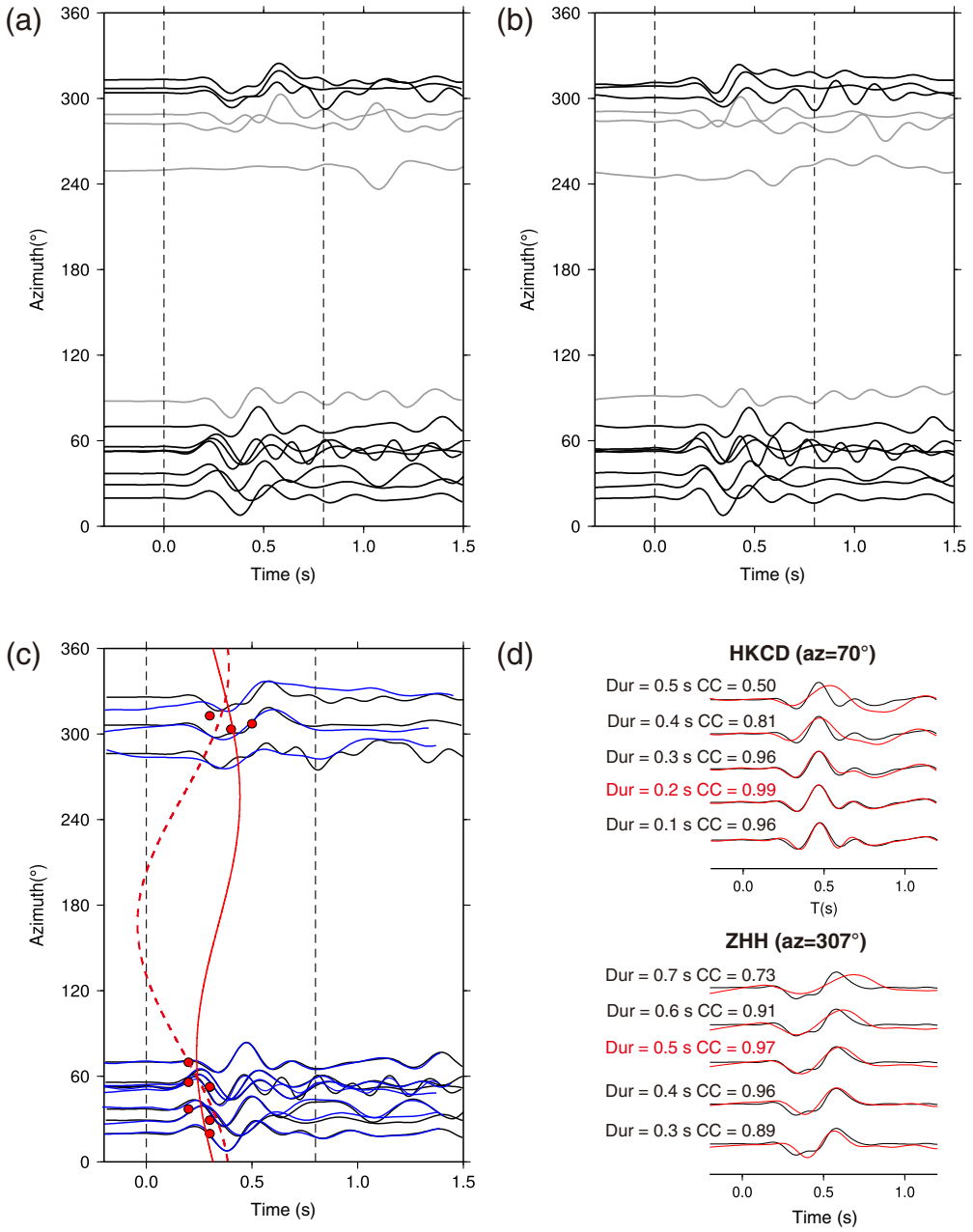

Figure 6. Rupture directivity analysis of the mainshock. (a) Low-pass filtered (5 Hz) vertical-component waveforms of the mainshock aligned to *P*-wave onset. Gray traces show the discarded data with CC coefficients lower than 0.8. Dashed lines indicate the time window in CC calculation. Panel (b) is the same as panel (a) but for the reference event. (c) Waveform comparison of the observed (black traces) and modeled seismograms (blue traces). Red dots show the resolved relative source duration, the red line shows the best-fitting prediction for NP1 by equation (3), and the red-dashed line shows that for NP2. The three traces with azimuth ~300° have been shifted to illustrate the waveforms better. (d) Waveform comparison of observed (black traces) and synthetic data (red traces) modeled with different source durations. The color version of this figure is available only in the electronic edition.

To obtain robust relative source durations, we performed forward modeling of the mainshock seismograms with the EGFs and source time functions (Fig. 6c). We generated source time functions with durations ranging from 0.1 to ~1.0 s and convolved them with the EGFs to match the waveforms of the mainshock. Then, we calculated CCs between the observed and synthetic data in a time window of 0.8 s to cover the direct *P* wave and suppress the coda waves. Nine stations with CCs coefficients larger than 0.8 were retained, and the resolved relative source durations ranged between 0.2 and 0.5 s. We then fitted the resolved relative source duration with equation (3) by the least-squares method. Because there is a large azimuthal gap (~180°) for the nine stations due to the offshore position, we could only resolve the fault plane, rupture length, and differential rise time, assuming that the rupture velocity and *P*-wave velocity were 2.5 and 6.0 km/s, respectively. Relative source durations of both NPs (78° and 168°) were calculated and fitted.

The fitting results (Fig. 6d) suggest that the mainshock ruptured toward northeast (78°) for about 0.6 km and the differential rise time was about 0.05 s. The resolved rupture length (0.6 km) was close to the prediction for an M_w 3.7 event (0.5 km) based on the scaling law (Gibson and Sandiford, 2013). The differential rise time (0.05 s) was also consistent with the predicted value (0.04 s). In comparison, the calculated source durations for NP2 were even negative at azimuths of 140°–200°, suggesting that the NP2 was not the ruptured plane.

Furthermore, we added random error (within ±0.1 s) to the relative source duration data at each station and fit the modified data with equation (3) for an additional 500 runs. The results show that (1) for 90.8% cases, the misfit of NP1 (78°) was smaller than that of NP2 (168°), indicating that the mainshock ruptured toward northeast; (2) the

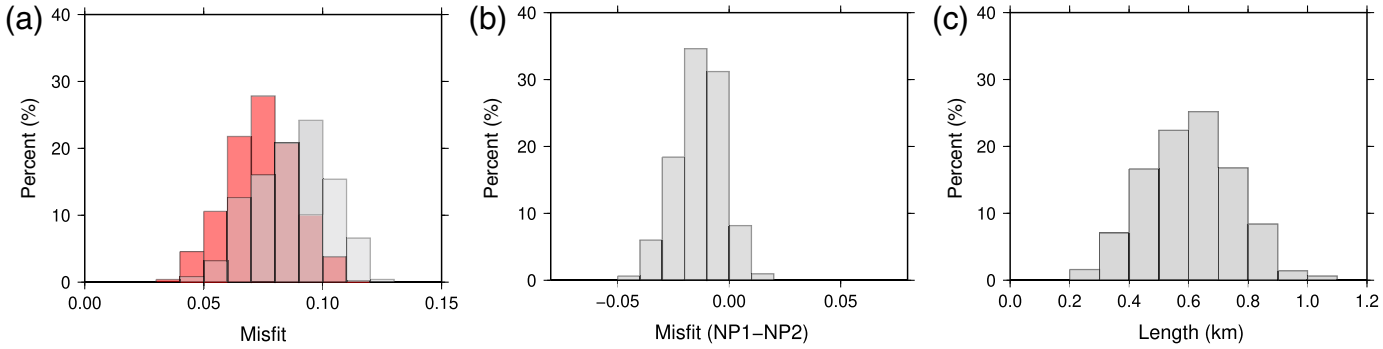

Figure 7. Uncertainty estimation of the rupture directivity analysis. (a) Histogram of the misfit of two NPs (red for NP1 [78°]; gray for NP2 [168°]). (b) Histogram of the misfit between NP1 and NP2. (c) Histogram of the resolved rupture length. The color version of this figure is available only in the electronic edition.

resolved rupture length ranged from 0.2 to 1.1 km, and thus the averaged rupture length was estimated as 0.6 km (Fig. 7a–c).

Discussion

By combining the focal mechanism solutions, the locations of the earthquakes, and the rupture directivity analysis, we suggest that the 4 January 2020 M_w 3.7 Zhuhai earthquake occurred on a northeast-east-trending strike-slip fault, with the orientation direction of 78°, which is consistent with the previously inferred northeast-east-trending faults. These faults offshore of PRE that were inferred from the gravity anomaly (Li *et al.*, 2006) were less convincing than near-coast faults traced according to inland faults or the large-scale LFZ with a more pronounced gravity anomaly. Our results provide the first direct evidence to confirm the distribution of one of the inferred faults. The 2020 M_w 3.7 earthquake enhances the interpretation that the northeast-east-trending fault system behaves as dextral strike-slip faults under the current north-west-west–northeast-east stress field in the northern SCS that was caused by the subduction of the Philippine Sea plate (Briais *et al.*, 1993).

Rupture propagation and extent are governed by many factors, such as fault geometry, heterogeneous stress distribution, and frictional properties on seismogenic faults (Weng and Yang, 2018; Yu *et al.*, 2018; Yang *et al.*, 2019; Yao and Yang, 2020). For strike-slip earthquakes, the eventual earthquake magnitudes are largely affected by the seismogenic width. The ruptures can become breakaway (i.e., breaking a large or full portion of a fault segment) and independent of the nucleation size when the seismogenic width is larger than the critical value of ~10 km (Weng and Yang, 2017). Our results show that these earthquakes are located at a depth of around 12 km. However, the results are insufficient to reveal the seismogenic width in the region because of the limited number of earthquakes. It is plausible that the seismogenic width of the faults is larger than the critical value because the focal depths of earthquakes in the past 10 yr in Guangdong's coastal region were distributed in depths of 5–20 km (Xia *et al.*, 2018). Thus, we cannot rule out the possibility that destructive strike-slip earthquakes may occur at the PRE. Further studies on the seismogenic width of faults are needed to better estimate the maximum magnitude earthquake in the PRE.

Conclusion

In this study, we conducted detailed investigations of source parameters for the 4 January 4th, 2020, earthquake in the PRE. The earthquake was followed by five aftershocks, all of which exhibited highly similar waveforms, indicating that they occurred on the same strike-slip fault. The results of rupture directivity analysis show that the 2020 M_w 3.7 Zhuhai earthquake occurred on a northeast-east-trending strike-slip fault, with the orientation direction of 78°. The fault coincided with the northeast-east-trending fault system in the offshore PRE region.

Data and Resources

Waveform data for this study are provided by Data Management Centre of China National Seismic Network at Institute of Geophysics (SEISDMC, DOI: 10.11998/SeisDmc/SN), China Earthquake Networks Center and GD Seismic Networks, China Earthquake Administration, Hong Kong Observatory Network, and Macau Observatory Network. We collected the five month seismograms of the HKPS station through the Incorporated Research Institutions for Seismology. The supplemental material for this article includes Supplementary Note 1 and Figures S1–S5. Data about Census and Statistics Department of Hong Kong are available at https://www.censtatd.gov.hk/hkstat/sub/sp150_tc.jsp?productCode=D5320189 (last accessed May 2020).

Acknowledgments

This work was supported by the Guangdong National Science Foundation (NSF) research team project (2017A030312002), Hong Kong Research Grant Council Grants (Numbers 14306418 and 14304820), Natural Science Foundation of China (NSFC) and Research Grants Council (RGC) Joint Research Scheme (N_CUHK430/16), Faculty of Science at The Chinese University of Hong Kong (CUHK), China Earthquake Science Experiment Project, China Earthquake Administration (CEA) (2017CESE0103, 2018CSES0101, 2018CSES0102, and 2019CSES0107), China Postdoctoral Science Foundation (Number 2019M663119), National Natural Science Foundation of China (Number 41804039), and Fundamental

Research Funds for Sun Yat-sen University (Number 20lgpy36). The figures were generated using the Generic Mapping Tool (GMT) software package (Wessel and Smith, 1991). The authors thank two anonymous reviewers for their constructive comments.

References

Assimaki, D., and S. Jeong (2013). Ground-motion observations at Hotel Montana during the M 7.0 2010 Haiti earthquake: Topography or soil amplification? *Bull. Seismol. Soc. Am.* **103,** no. 5, 2577–2590, doi: 10.1785/0120120242.

Atkinson, G. M., and J. F. Cassidy (2000). Integrated use of seismograph and strong-motion data to determine soil amplification: Response of the Fraser River delta to the Duvall and Georgia Strait earthquakes, *Bull. Seismol. Soc. Am.* **90,** no. 4, 1028–1040.

Bhattacharyya, R., P. Verma, and T. Majumdar (2009). High resolution satellite geoids/gravity over the western Indian offshore for tectonics and hydrocarbon exploration, *Indian J. Geomarine Sci.* **38,** no. 1, 116–125.

Briais, A., P. Patriat, and P. Tapponnier (1993). Updated interpretation of magnetic anomalies and seafloor spreading stages in the South China Sea: Implications for the Tertiary tectonics of southeast Asia, *J. Geophys. Res.* **98,** no. B4, 6299–6328.

Cao, J., S. Xia, J. Sun, F. Zhao, K. Wan, and H. Xu (2018). Offshore fault geometrics in the Pearl River Estuary, southeastern China: Evidence from seismic reflection data, *J. Ocean Univ. China* **17,** no. 4, 799–810, doi: 10.1007/s11802-018-3499-5.

Chau, K., R. Wong, Y. Wong, K. Lai, L. Wang, Y. Chan, W. Wong, Y. Guo, W. Zhu, and S. Zheng (2004). Three-dimensional surface cracking and faulting in Dangan islands area, South of Hong Kong, *Proc. of Third International Conf. on Continental Earthquakes*, Beijing, China, 60 pp.

Chen, Q. C., T. Y. Fan, X. S. Li, S. L. He, C. Y. Zhang, and W. Meng (2014). In situ measurements and comprehensive research on the present crustal stress of northern South China Sea, *Chin. J. Geophys.* **57,** no. 4, 462–473.

Chen, R., Y. Kang, X. Huang, X. Yang, and Y. Ding (2009). Seismic risk analysis in northern South China Sea, *South China J. Seismol.* **29,** no. 4, 36–45.

Dong, H. (2016). The basic features of Shawan fault and analysis of the coupling with the landform, *Geol. Miner. Resour. South China* **32,** no. 3, 238–248 (in Chinese).

Fan, Y., J. Lin, R. Hu, and Z. Luo (1990). The development of travel timetable for near earthquake in South China, *South China Seismol. J.* **10,** no. 2, 1–16 (in Chinese).

Fichler, C., E. Rundhovde, S. Johansen, and B. Sæther (1997). Barents Sea tectonic structures visualized by ERS1 satellite gravity data with indications of an offshore Baikalian trend, *First Break* **15,** no. 11, doi: 10.1046/j.1365-2397.1997.00678.x.

Free, M., J. Pappin, and R. Koo (2004). Seismic hazard assessment in a moderate seismicity region, Hong Kong, *Proc. of the 13th World Conf. on Earthquake Engineering*, 1–6 August, Paper Number 1659.

Fu, J., D. Jiang, and Y. Huang (2014). 1 km grid population dataset of China (2005, 2010), *Acta Geogr. Sin.* **69,** 136–139.

Fukuyama, Y. (2002). Fundamentals of particle swarm techniques, in *Modern Heuristic Optimization Techniques with Applications to Power Systems*, K. Y. Lee and M. A. El-Sharkawi (Editors), 45–51.

Galvis, F., E. Miranda, P. Heresi, H. Dávalos, and J. R. Silos (2017). Preliminary statistics of collapsed buildings in Mexico City in the September 19th, 2017 Puebla-Morelos earthquake, *John A. Blume Earthquake Engineering Center and Department of Civil and Environmental Engineering Stanford University*, available at http://learningfromearthquakes.org (last accessed December 2020).

Gangopadhyay, A., and P. Talwani (2003). Symptomatic features of intraplate earthquakes, *Seismol. Res. Lett.* **74,** no. 6, 863–883.

Gibson, G., and M. Sandiford (2013). Seismicity and induced earthquakes, *Background Paper to NSW Chief Scientist and Engineer (OCSE)*, Univ. Melbourne, 33 pp.

Ghobarah, A., M. Saatcioglu, and I. Nistor (2006). The impact of the 26 December 2004 earthquake and tsunami on structures and infrastructure, *Eng. Struct.* **28,** no. 2, 312–326, doi: 10.1016/j.engstruct.2005.09.028.

Grant, L. B., and P. M. Shearer (2004). Activity of the offshore Newport–Inglewood Rose Canyon fault zone, coastal southern California, from relocated microseismicity, *Bull. Seismol. Soc. Am.* **94,** no. 2, 747–752.

Guangdong Seismological Bureau (2011). *Earthquake Prevention and Disaster Reduction in 12th five-year Plan of Guangdong Province*, Guangdong Seismological Bureau, Guangzhou, China, 4–20.

Guo, Q., J. Zheng, Z. Liang, and L. Li (1995). Prediction of site earthquake hazard in the Pearl River delta area, *South China J. Seismol.* **3,** 3.

Hanks, T. C., and D. M. Boore (1984). Moment-magnitude relations in theory and practice, *J. Geophys. Res.* **89,** no. B7, 6229–6235.

Hao, T., S. Mancheol, and Q. Wang (2002). A study on the extension of fault zones in Yellow Sea and its adjacent areas based on gravity data, *Chin. J. Geophys.* **45,** no. 3, 385–397.

Hartzell, S. H. (1978). Earthquake aftershocks as Green's functions, *Geophys. Res. Lett.* **5,** no. 1, 1–4.

Hsiao, L.-Y., S. A. Graham, and N. Tilander (2004). Seismic reflection imaging of a major strike-slip fault zone in a rift system: Paleogene structure and evolution of the Tan-Lu fault system, Liaodong Bay, Bohai, offshore China, *AAPG Bulletin* **88,** no. 1, 71–97, doi: 10.1306/09090302019.

Hunter, J., and H. Christian (2001). Use of shear wave velocities to estimate thick soil amplification effects in the Fraser River delta, British Columbia, *14th EEGS Symposium on the Application of Geophysics to Engineering and Environmental Problems*, European Association of Geoscientists & Engineers, Denver, Colorado, 4–7 March.

Kennett, B., and E. Engdahl (1991). Traveltimes for global earthquake location and phase identification, *Geophys. J. Int.* **105,** no. 2, 429–465.

Klein, F. W. (2002). User's guide to HYPOINVERSE-2000, a Fortran program to solve for earthquake locations and magnitudes, *U.S. Geol. Surv. Open-File Rept. 2002-171*, 123 pp.

Lee, C., and D. Workman (1996). Earthquakes in the South China region and their impact on Hong Kong, *Seismicity in Eastern Asia, Geological Society of Hong Kong Bulletin No. 5*, R. B. Owen, R. J. Neller, and K. W. Lee (Editors), 92–103.

Lee, C., Y. Ding, and X. Huang (2000). Seismic hazard analysis of the Hong Kong region, *J. Seismol. Earthq. Eng.* **2,** no. 4, 9–18.

Li, F., Z. Sun, and H. Yang (2018). Possible spatial distribution of the Mesozoic volcanic arc in the present-day South China Sea

continental margin and its tectonic implications, *J. Geophys. Res.* **123,** 6215–6235, doi: 10.1029/2017JB014861.

Li, F., Z. Sun, H. Yang, J. Lin, J. M. Stock, Z. Zhao, H. Xu, and L. Sun (2020). Continental interior and edge breakup at convergent margins induced by subduction direction reversal: A numerical modeling study applied to the South China Sea margin, *Tectonics* **39,** e2020TC006409, doi: 10.1029/2020TC006409.

Li, G., B. Liu, J. Wu, X. Li, and G. Han (2006). Fault structure features in the southern Lingdingyang Sea area, *Adv. Mar. Sci.* **24,** no. 3, 320.

Liu, Y. (1985). The active fractures in South China coast, *Mar. Geol. Quaternary Geol.* **5,** no. 3, 11–21.

Liu, Y. (1986). Basic features and activity discussion of Nanao fault zone and littoral fault zone, *South China J. Seismol.* **6,** no. 3, 1–8.

Liu, Z., Y. Zhao, Y. Zhang, X. Zhou, S. He, Y. Xie, S. Jiang, Q. Wang, Z. Huang, and J. Lin (1997). A comprehensive study on Zhujiang River Mouth–Liyue Bank–Nansha trough transect in the South China Sea, *Nanhai Studia Marina Sin.* **12,** 1–24.

Megawati, K. (2007). Hybrid simulations of ground motions from local earthquakes affecting Hong Kong, *Bull. Seismol. Soc. Am.* **97,** no. 4, 1293–1307.

Megawati, K., N. T. Lam, A. M. Chandler, and T.-C. Pan (2004). Cities without a seismic code: hazard assessment, *Proc. of the 13th World Conf. on Earthquake Engineering*, Vancouver, B.C., Canada, 1–6 August, Paper Number 129.

Meng, X., H. Yang, and Z. Peng (2018). Foreshocks, *b* value map, and aftershock triggering for the 2011 M_w 5.7 Virginia earthquake, *J. Geophys. Res.* **123,** no. 6, 5082–5098.

Mimura, N., K. Yasuhara, S. Kawagoe, H. Yokoki, and S. Kazama (2011). Damage from the Great East Japan earthquake and tsunami—A quick report, *Mitig. Adapt. Strateg. Glob. Change* **16,** no. 7, 803–818, doi: 10.1007/s11027-011-9297-7.

Pappin, J. W., R. C. H. Koo, H. Jiang, J. S. H. Kwan, Y. B. Yu, M. M. L. So, Y. K. Shiu, K. K. S. Ho, and W. K. Pun (2015). A rigorous probabilistic seismic hazard model for southeast China: A case study of Hong Kong, *Bull. Earthq. Eng.* **13,** no. 12, 3597–3623, doi: 10.1007/s10518-015-9798-y.

Pigott, J. D., and K. Ru (1994). Basin superposition on the northern margin of the South China Sea, *Tectonophysics* **235,** nos. 1/2, 27–50.

Saito, K., R. J. Spence, C. Going, and M. Markus (2004). Using high-resolution satellite images for post-earthquake building damage assessment: A study following the 26 January 2001 Gujarat earthquake, *Earthq. Spectra* **20,** no. 1, 145–169.

Schaff, D. P., and P. G. Richards (2014). Improvements in magnitude precision, using the statistics of relative amplitudes measured by cross correlation, *Geophys. J. Int.* **197,** no. 1, 335–350, doi: 10.1093/gji/ggt433.

Sepahi, M. N., B. Maskare, M. Boomeri, P. Gadpallu, and R. A. Duraiswami (2020). Ground fracturing related to 7.8 M_w Saravan earthquake, Sistan and Baluchistan, Iran—Evidence for brittle deformation, *J. Geol. Soc. India* **95,** no. 4, 343–349, doi: 10.1007/s12594-020-1442-z.

Shelly, D. R., W. L. Ellsworth, and D. P. Hill (2016). Fluid-faulting evolution in high definition: Connecting fault structure and frequency–magnitude variations during the 2014 Long Valley Caldera, California, earthquake swarm, *J. Geophys. Res.* **121,** no. 3, 1776–1795, doi: 10.1002/2015jb012719.

Sheng, M., R. Chu, Y. Wang, and Q. Wang (2020). Inversion of source mechanisms for single-force events using broadband waveforms, *Seismol. Res. Lett.* **91,** 1820–1830.

Stefatos, A., G. Papatheodorou, G. Ferentinos, M. Leeder, and R. Collier (2002). Seismic reflection imaging of active offshore faults in the Gulf of Corinth: Their seismotectonic significance, *Basin Res.* **14,** no. 4, 487–502.

Sun, J., H. Xu, W. Zhan, and J. Cao (2012). Activity and triggering mechanism of seismic belt along the northern South China Sea continental margin, *J. Trop. Oceanogr.* **31,** no. 3, 40–47.

Tan, M., Y. Qiu, and H. Zou (2000). Regional tectonic study in the Coastal of Guangdong, *Geol. Miner. Explor. Bur. Guangzhou* 45–71.

Tan, Y., and D. Helmberger (2010). Rupture directivity characteristics of the 2003 big bear sequence, *Bull. Seismol. Soc. Am.* **100,** no. 3, 1089–1106, doi: 10.1785/0120090074.

Tichelaar, B. W., and L. J. Ruff (1989). How good are our best models? Jackknifing, bootstrapping, and earthquake depth, *Eos Trans. AGU* **70,** no. 20, 593–606.

Waldhauser, F., and W. L. Ellsworth (2000). A double-difference earthquake location algorithm: Method and application to the northern Hayward fault, California, *Bull. Seismol. Soc. Am.* **90,** no. 6, 1353–1368.

Wei, B., H. Xu, and M. Xie (1996). Recent tectonic stress field in the southeast China coastal seismic zone, *South China J. Seismol.* **16,** 12–19 (in Chinese).

Weng, H., and H. Yang (2017). Seismogenic width controls aspect ratios of earthquake ruptures, *Geophys. Res. Lett.* **44,** no. 6, 2725–2732.

Weng, H., and H. Yang (2018). Constraining frictional properties on fault by dynamic rupture simulations and near-field observations, *J. Geophys. Res.* **123,** 6658–6670, doi: 10.1029/2017JB015414.

Wessel, P., and W. H. Smith (1991). Free software helps map and display data, *Eos, Trans. AGU* **72,** no. 41, 441–446.

Xia, S., J. Cao, J. Sun, J. Lv, H. Xu, X. Zhang, K. Wan, C. Fan, and P. Zhou (2018). Seismogenic structures of the 2006 M_L 4.0 Dangan Island earthquake offshore Hong Kong, *J. Ocean Univ. China* **17,** no. 1, 169–176, doi: 10.1007/s11802-018-3452-7.

Xia, S., M. Zhao, X. Qiu, H. Xu, and X. Shi (2010). Crustal structure in an onshore–offshore transitional zone near Hong Kong, northern South China Sea, *J. Asian Earth Sci.* **37,** nos. 5/6, 460–472, doi: 10.1016/j.jseaes.2009.11.004.

Xu, H., X. Qiu, M. Zhao, J. Sun, and J. Zhu (2006). Characteristics of the crustal structure and hypocentral tectonics in the epicentral area of Nan'ao earthquake (M7.5), the northeastern South China Sea, *Chin. Sci. Bull.* **51,** no. S2, 95–106, doi: 10.1007/s11434-006-9095-x.

Yang, H. (2015). Recent advances in imaging crustal fault zones: A review, *Earthq. Sci.* **28,** no. 2, 151–162.

Yang, H., S. Yao, B. He, and A. V. Newman (2019). Earthquake rupture dependence on hypocentral location along the Nicoya Peninsula subduction megathrust, *Earth Planet. Sci. Lett.* **520,** 10–17.

Yang, H., L. Zhu, and R. Chu (2009). Fault-plane determination of the 18 April 2008 Mount Carmel, Illinois, earthquake by detecting and relocating aftershocks, *Bull. Seismol. Soc. Am.* **99,** no. 6, 3413–3420, doi: 10.1785/0120090038.

Yao, S., and H. Yang (2020). Rupture dynamics of the 2012 Nicoya M_w 7.6 earthquake: Evidence for low strength on the megathrust, *Geophys. Res. Lett.* **47,** e2020GL087508, doi: 10.1029/2020GL087508.

Yu, C. Q., K. Tao, X. F. Cui, X. P. Hu, and J. Y. Ning (2009). *P*-wave first-motion focal mechanism solutions and their quality evaluation, *Chin J. Geophys.* **52,** no. 5, 1402–1411.

Yu, H., Y. Liu, H. Yang, and J. Ning (2018). Modeling earthquake sequences along the Manila subduction zone: Effects of three-dimensional fault geometry, *Tectonophysics* **733,** 73–84, doi: 10.1016/j.tecto.2018.01.025.

Yu, Z., K. Zhang, H. Liang, and Z. Li (2016). Late Quaternary tectonic movements in the Pearl River delta, China, revealed from stratigraphic profiles, *Tropical Geogr.* **36,** no. 3, 334–342.

Zhang, H. N., and Q. Wu (1994). A comparative study of main active fault zones along the coast of South China, *Seismol. Geol.* **16,** no. 1, 43–52.

Zhao, M. H., X. L. Qiu, C. M. Ye, K. Y. Xia, C. L. Huang, J. B. Xie, P. Wang, and L. T. Sun (2004). An analysis on deep crustal structure along the onshore–offshore seismic profile across the Binghai (Littoral) fault zone in Ne South China Sea, *Chin. J. Geophys.* **47,** no. 5, 954–961.

Zhu, G., H. Yang, J. Lin, Z. Zhou, M. Xu, J. Sun, and K. Wan (2019). Along-Strike variation in slab geometry at the southern Mariana subduction zone revealed by seismicity through ocean bottom seismic experiments, *Geophys. J. Int.* **218,** no. 3, 2122–2135.

Zhu, L., and D. V. Helmberger (1996). Advancement in source estimation techniques using broadband regional seismograms, *Bull. Seismol. Soc. Am.* **86,** no. 5, 1634–1641.

Zhu, L., and L. A. Rivera (2002). A note on the dynamic and static displacements from a point source in multilayered media, *Geophys. J. Int.* **148,** no. 3, 619–627.

Manuscript received 7 July 2020
Published online 6 January 2021